INTERNATIONAL JOURNAL FOR NUMERICAL METHODS IN FLUIDS
Int. J. Numer. Meth. Fluids **30**: 43–63 (1999)

FREE-SURFACE FLOW OVER A SEMI-CIRCULAR OBSTRUCTION

KRISTEN LOWERY[1] AND STERGIOS LIAPIS*[,2]

Aerospace and Ocean Engineering, Virginia Polytechnic Institute and State University, Blacksburg, VA 24061, USA

SUMMARY

The fully non-linear free-surface flow over a semi-circular bottom obstruction was studied numerically in two dimensions using a mixed Eulerian–Lagrangian formulation. The problem was solved in the time domain that allows the prediction of a number of transient phenomena, such as the generation of upstream advancing solitary waves, as well as the simulation of wave breaking. A parametric study was performed for a range of values of the depth-based Froude number up to 2.5 and non-dimensional obstacle heights, α up to 0.9. When wave breaking does not occur, three distinct flow regimes were identified: subcritical, transcritical and supercritical. When breaking occurs it may be of any type: spilling, plunging or surging. In addition, for values of the Froude number close to 1, the upstream solitary waves break. A systematic study was undertaken to define the boundaries of each type of breaking and non-breaking pattern and to determine the drag and lift coefficients, free-surface profile characteristics and transient behavior. Copyright © 1999 John Wiley & Sons, Ltd.

KEY WORDS: Eulerian–Lagrangian formulation; free-surface flow; semi-circular obstruction

1. INTRODUCTION

The fully non-linear, free-surface, two-dimensional potential flow of an incompressible fluid over a semi-circular bottom obstruction is analyzed. The flow, a sufficient distance ahead of the obstruction, has a uniform velocity and depth. This problem may be described in terms of two non-dimensional parameters. A depth-based Froude number is defined as $Fn \equiv U_B/\sqrt{g \cdot h}$, where U_B is the uniform upstream velocity, h is the uniform upstream depth and g is the gravitational acceleration. The non-dimensional obstruction height is given as $\alpha \equiv R/h$, where R is the radius of the obstacle. The steady flow over an obstacle has been studied by a number of investigators (Forbes [1], Forbes and Schwartz [2], Zhang and Zhu [3], Vanden-Broeck [4], Houghton and Kasahara [5] and Lawrence [6]). The steady state response of the free-surface can be typified into certain flow regimes depending on the upstream depth-based Froude number and the non-dimensional obstruction height. These regimes have common free-surface characteristics, and are depicted in Figure 1. Five distinct patterns for the free-surface behavior at steady state have been identified. These are: subcritical, supercritical, partially blocked with no lee (downstream) hydraulic jump, partially blocked with a lee hydraulic jump, and complete blocking. Houghton and Kawahara [5] and Lawrence [6] developed equations defining the

---

* Correspondence to: Shell E&P Tech. Co., Bellaire Tech. Center, PO Box 481, Houston, TX 77001-0481, USA.

[1] Current address: Aker Engineering, 11767 Katy Freeway, Suite 1300, Houston, TX 77079, USA.

[2] Current address: Offshore Structures, Shell Oil Company, 3737 Bellaire Blvd., Houston, TX 77001, USA.

CCC 0271–2091/99/090043–21$17.50

Received 20 July 1997
Revised 11 May 1998

boundaries between the various flow regimes. In a recent study, Zhu and Zhang [7] formulated the same problem in the time domain. However, due mainly to the absence of open boundary conditions, they were able to obtain numerical results only for values of the Froude number greater than 1.

While the steady models have been useful in identifying some key features of the fluid problem, for certain speeds, even though the conditions are steady, the flow never reaches a steady state. This is related to the generation of unsteady solitary waves propagating upstream of the obstacle. This phenomenon occurs for a number of disturbances in a uniform flow, such as a free-surface pressure distribution or a ship, and has been identified by a number of authors. While Thews and Landweber [8] are credited with first mentioning this phenomenon, systematic studies of this phenomenon are much more recent. Wu and Wu [9] used a generalized Boussinesq model for long waves generated by a moving pressure or bottom obstacle. The same phenomenon was studied using the Korteweg–de Vries (KdV) equation by Akylas [10], Cole [11] and Mei [12]. Ertekin *et al.* [13] reported analytical results using the Green–Naghdi theory as well as experimental results. In a recent study, Cao *et al.* [14] presented numerical computations of two-dimensional solitary waves generated by moving disturbances using a desingularized boundary integral method.

In this paper, the free-surface flow over a bottom obstruction is studied numerically. Unlike the previous studies, the problem is solved in the time domain. Transient, fully non-linear computations were performed using a mixed Eulerian–Lagrangian formulation. Unlike the

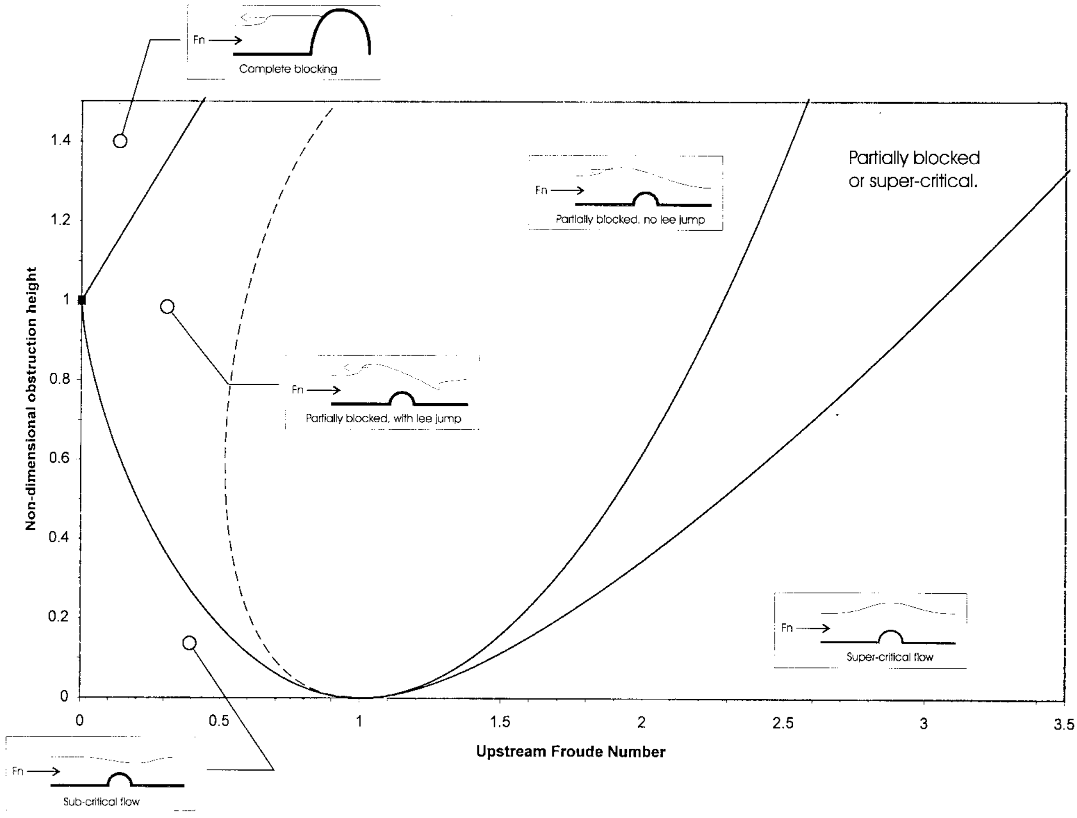

Figure 1. The steady state flow regimes.

Boussinesq or the KdV formulations that are restricted to cases where the velocity varies slowly with the depth, the present numerical computations can handle arbitrary velocity variations with depth. A numerical towing tank with open boundary conditions on the upstream and downstream vertical boundaries has been developed to perform this study. The computer simulation 'tows' the semi-circular bottom obstruction from rest to a steady Froude number. The program determines the free-surface elevation, calculates the force coefficients, and determines the energy in the tank at each time step. The data for the response of the free-surface is translated to a co-ordinate frame moving with the structure to show how the free-surface develops over time. In addition to computing the upstream solitary waves, which confirm the findings of the approximate theories, this procedure allows the simulation of wave breaking.

A parametric study was performed for a range of values of the Froude number up to 2.5 and non-dimensional obstacle heights, α up to 0.9. The boundary line separating the breaking and non-breaking wave regimes was obtained. When wave breaking does not occur, three distinct flow regimes were identified: subcritical, transcritical and supercritical. When breaking occurs it may be of any type: spilling, plunging or surging. In addition, for a range of values of the Froude number close to 1, the upstream solitary waves break. A systematic study was undertaken to define the boundaries of each type of breaking and non-breaking pattern. In addition, the time histories of the drag and lift coefficients, as well as the free-surface elevation, were obtained. Several features of the fluid flow were very different than what was predicted by the steady flow models. To the authors knowledge, while there have been quite a few steady state studies of this problem, this is the first complete study of this problem in the time domain.

2. TWO-DIMENSIONAL FLUID FLOW PARAMETRIC STUDY

2.1. Mathematical formulation

The unsteady, two-dimensional potential flow of an inviscid, incompressible fluid induced by a bottom obstacle moving at a constant speed U along the fluid bottom is analyzed. Under the usual assumptions of a two-dimensional, inviscid, irrotational flow, the problem may be described by a velocity potential ϕ and a streamfunction ψ. A Cartesian x–y system is defined with y positive upward and the x-axis coinciding with the undisturbed free-surface. Non-dimensional variables are chosen so that the initial fluid depth, the acceleration of gravity and the fluid density are equal to one. In the fluid domain R, the velocity potential ϕ must satisfy the Laplace equation:

$$\nabla^2\phi = 0. \tag{1}$$

On the free-surface C_{F}, the kinematic boundary conditions are

$$\frac{\mathrm{D}x}{\mathrm{D}t} = \frac{\partial\phi}{\partial x} \quad \text{and} \quad \frac{\mathrm{D}y}{\mathrm{D}t} = \frac{\partial\phi}{\partial y} \tag{2}$$

and the dynamic free-surface condition is given by the Bernoulli equation:

$$\frac{\mathrm{D}\phi}{\mathrm{D}t} = -\eta + \frac{(\nabla\phi)^2}{2}, \tag{3}$$

where D is the substantial derivative, x and y are the co-ordinates of the position of a fluid particle, and η is the free-surface elevation.

On the bottom obstacle surface C_S, the fluid flow satisfies the no-penetration condition:

$$\frac{\partial \phi}{\partial n} = -U_B n_1, \tag{4}$$

where U_B is the velocity of the obstacle, and n_1 is the x-component of the unit normal to the surface.

On the flat bottom C_B, one has

$$\frac{\partial \phi}{\partial n} = 0. \tag{5}$$

The complex variable $z = x + iy$ and the complex velocity potential, β ($\beta(z) = \phi(z) + i\psi(z)$), are introduced. Since β is analytical in the fluid domain, it satisfies the Cauchy integral theorem:

$$\oint_C \frac{\beta(z)}{(z - z_k)} \mathrm{d}z = 0 \quad \text{for } z_k \text{ outside the fluid domain} \tag{6a}$$

$$\oint_C \frac{\beta(z)}{(z - z_k)} \mathrm{d}z = -i\alpha_k \beta(z_k) \quad \text{for } z_k \text{ on the fluid boundary} \tag{6b}$$

$$\oint_C \frac{\beta(z)}{(z - z_k)} \mathrm{d}z = 2\pi i \beta(z_k) \quad \text{for } z_k \text{ inside the fluid domain} \tag{6c}$$

where the contour C consists of the free-surface C_F, the bottom C_B, the obstacle surface C_S and the upstream and downstream boundaries. The contour C is traversed such that the region R always lies to its left and α_k is the angle between two elements adjacent to z_k on the contour. For a smooth contour $\alpha_k = -\pi$.

A mixed Eulerian–Lagrangian formulation is employed to solve the boundary value problem (1)–(5). This method has been used very successfully to predict a variety of non-linear wave phenomena by a number of investigators (Longuet-Higgins and Cokelet [15], Vinje and Brevig [16], Lin *et al.* [17], Cointe [18], Muthedath [19]). This method involves an Eulerian and a Lagrangian step. At each instant of time, the integral equation (6b) is solved numerically (the Eulerian step). On some portions of the boundary φ is known, while on others ψ is known. On the free-surface φ is given by Equation (3), while on the flat bottom ψ is zero and on the bottom obstacle surface ψ is given by Equation (4). After solving the boundary value problem at each time step, the free-surface conditions (2) and (3) are stepped forward in time to update the positions and the values of the velocity potential of particles of fixed identity (the Lagrangian step).

2.1.1. Numerical implementation. The boundary C is divided into elements (panels). Figure 2 shows the layout of the tank and boundary elements. Within each panel the complex potential $\beta(z)$ is assumed to vary linearly with z. This can be expressed as:

$$\beta(z) = \frac{z - z_j}{z_{j-1} - z_j} \beta_{j-1} + \frac{z - z_{j-1}}{z - z_{j-1}} \beta_j. \tag{7}$$

This approximation of $\beta(z)$ reduces the problem of finding a continuous potential to determining the unknown nodal values β_j. These are found by collocation, i.e. by satisfying the integral equation (6b) at the panel vertices.

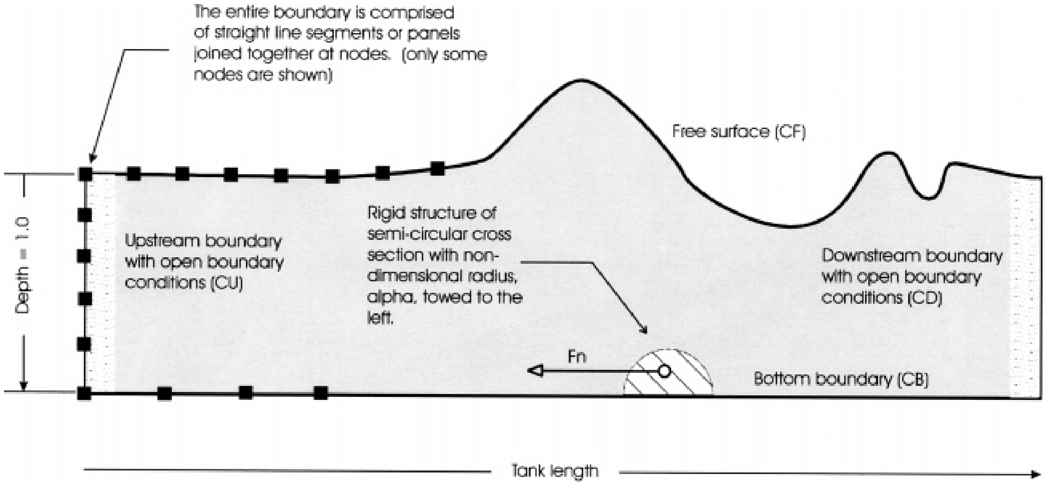

Figure 2. Numerical towing tank layout.

Detailed accuracy and convergence tests were carried out to determine the numerical tank length, the panel arrangement and the time step size for the numerical simulations. After trial and error, the tank length was chosen equal to 75 times the depth. A total of 508 panels are used for the simulations presented here; 299 panels are used on the free-surface. There are five panels on each of the vertical ends, 179 panels make up the flat bottom boundary and are arranged so that 90 panels are to the left of the obstruction and 89 are to the right of the obstruction. The remaining 20 panels define the surface of the obstruction.

The obstruction is translated towards the left end of the tank, in the negative x-direction. As the obstacle moves, the flat bottom segments to either side change in length accordingly. To maintain equal panel lengths over each of these segments, the nodes are redistributed at each time step. The nodes on the vertical boundaries are also redistributed at each time step to retain equal panel lengths.

Time stepping of the boundary value problem is performed by Hamming's fourth-order predictor–corrector method. A Runge–Kutta fourth-order method is employed for the first four time steps to provide the initial data for use in Hamming's method. A non-dimensional time step of 0.05 is used. The structure is started from rest with a velocity ramp. During this acceleration phase, the velocity is gradually increased in a linear fashion to its final value. It was found that a velocity increase of 0.05 *Fn* per time step provides a smooth start-up.

Nodes on the free-surface are smoothed every five time steps using a fifth-order smoothing formula developed by Longuet-Higgins and Cokelet [15]:

$$\bar{y}_i = \frac{1}{16}(-y_{i-2} + 4y_{i-1} + 10y_i + 4y_{i+1} - y_{i+2}), \tag{8}$$

where the subscript i indicates the ith node, $i-1$ is the previous node and so forth. Smoothing is necessary to suppress short wave, saw-tooth instabilities that are related to numerical error. Such instabilities occur mostly in the case of breaking waves where the local wave steepness is large. This formula works very well and suppressed all saw-tooth instabilities seen in this study. No adverse effects of smoothing, such as the introduction of numerical damping or dissipation to the numerical solution, were observed.

2.1.2. Far-field boundary conditions. A satisfactory treatment of the upstream and downstream boundaries is of fundamental importance to the success of the numerical simulations. The early studies of non-linear breaking waves assumed spatial periodicity in x, this scheme, however, breaks down at large times. In the simulations of Zhu and Zhang [7], rigid-wall boundary conditions were imposed at the upstream and downstream boundaries. As a result, they were unable to carry out numerical simulations of the problem in the subcritical and transcritical regions Boundary conditions allowing the waves to leave the computational domain without any reflection are of great interest and have generated a lot of literature. No general method has yet been proposed for the radiation of fully non-linear waves. Examples of some very recent studies include Grilli and Horrillo [20] and Van Dongeren and Svendsen [21]. In this work, Sommerfeld radiation conditions are imposed both at the upstream and downstream boundaries in a manner similar to what has been used in other problems (Orlanski [22]), i.e. one requires:

$$\frac{\partial\psi}{\partial t}\pm c\frac{\partial\psi}{\partial x}=0, \tag{9}$$

where c is the local wave velocity and the + and − signs apply to the downstream and upstream boundaries respectively. These conditions make the upstream and downstream boundaries transparent to all linear or weakly non-linear waves of velocity c, thus eliminating reflections. The local wave velocity c in the general case is unknown. In the present study, c is set equal to the phase velocity $(gh)^{1/2}=1$ (unit depth and gravitational acceleration have been assumed). Some authors (Han *et al.* [23]) suggested a numerical method of calculating c. This numerical method involves adding a column of points just inside the upstream and downstream boundaries. Then a finite difference scheme is employed to find the spatial and temporal derivatives of $\beta(z)$ and Equation (9) is used to give the velocity c. The authors tested this scheme using both first- and second-order difference schemes to approximate the derivatives of $\beta(z)$ but found that the simple choice of $c=(gh)^{1/2}$ is superior and reduces the reflected waves to a minimum.

The numerical method used to implement Equation (9) involves adding a column of points just inside the upstream and downstream boundaries. Then a finite difference scheme is employed to find the spatial and temporal derivatives of $\psi(z)$. For the time derivative, a backward difference scheme was used. For the spatial derivative, a forward difference scheme was used. This gives:

$$\frac{\psi(x_u, y_u, t)-\psi(x_u, y_u, t-\Delta t)}{\Delta t}+c\,\frac{\psi(x_u+\Delta x, y_u, t-\Delta t)-\psi(x_u, y_u, t-\Delta t)}{\Delta x}=0.$$

Rearranging to determine the nodal value of $\psi(x_u, y_u, t)$,

$$\psi(x_u, y_u, t)=\psi(x_u, y_u, t-\Delta t)-c\,\frac{\Delta t}{\Delta x}\,[\psi(x_u+\Delta x, t-\Delta t)-\psi(x_u, y_u, t-\Delta t)], \tag{10}$$

where x_u, y_u are the co-ordinates of a node on the upstream boundary ($x_u=0$), t is the current time in the simulation, Δt is the time step interval and Δx is the distance of the additional points from the upstream boundary. The value of Δx used was 5 times the upstream depth. At each time step $(t-\Delta t)$ after solving for the value of ψ on the boundary nodes, the value of ψ on the interior points, $\psi(x_u+\Delta x, y_u, t-\Delta t)$ is determined using Equation (6c). Then Equation (10) is used to update the value of $\psi(x_u, y_u, t)$ at the nodes making up the upstream boundary at each time step. As an example, Figure 3 shows the free-surface profile for a non-dimensional obstacle height of 0.2 and a Froude number of 0.1. Both cases of open boundary conditions

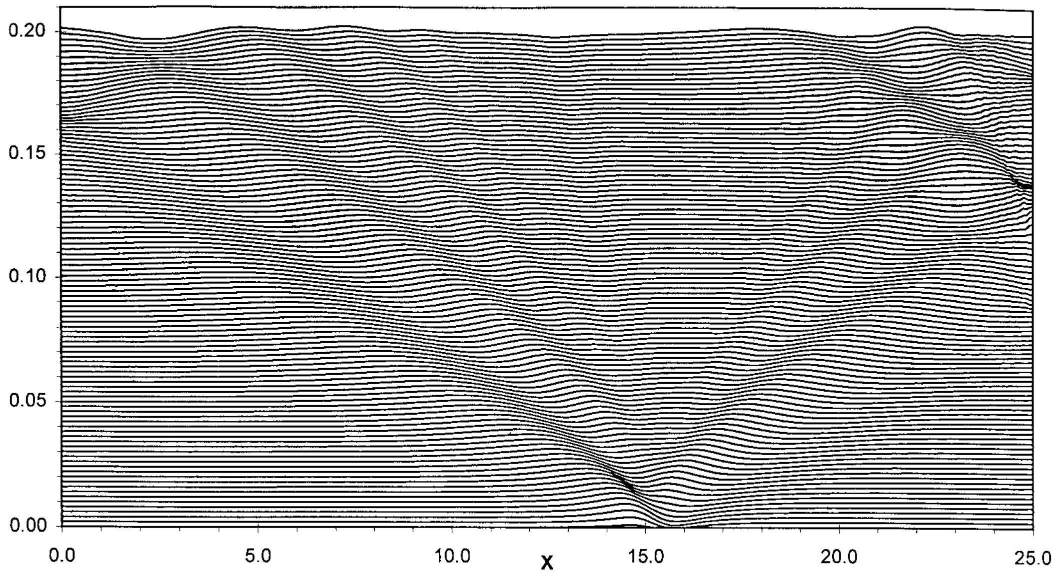

Free surface profile for a towing tank with solid walls on the upstream and downstream boundaries. The small obstacle is located at x=15. The flow is from left to right at a Froude number of 0.1. The non-dimensional obstacle height is 0.2.

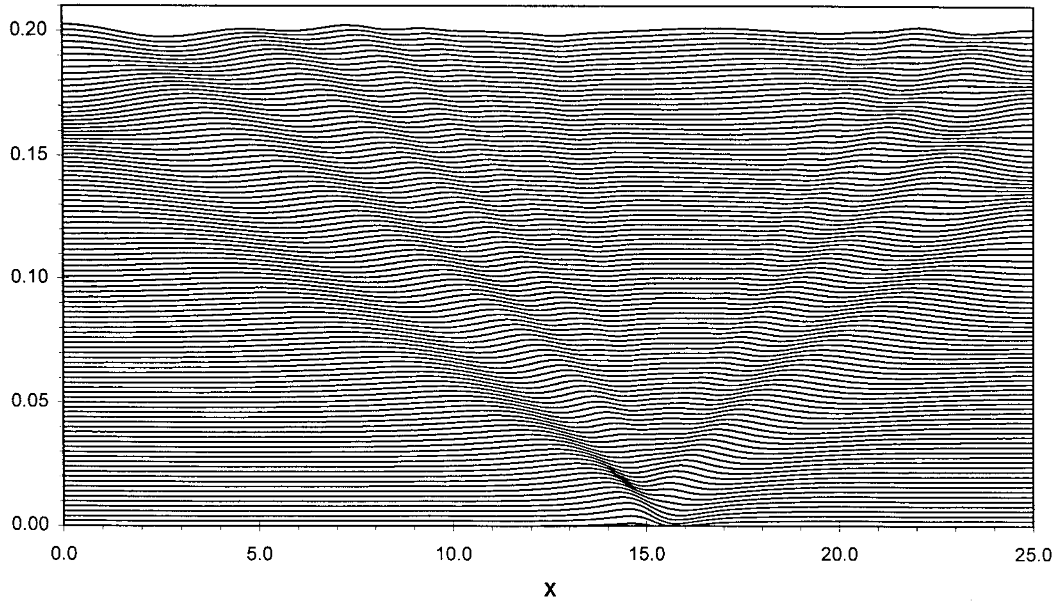

Free surface profile for a towing tank with open boundary conditions upstream and downstream. The small obstacle is located at x=15. The flow is from left to right at a Froude number of 0.1. The non-dimensional obstacle height is 0.2.

Figure 3. Comparison of the results with and without open boundary conditions at the vertical boundaries of the towing tank.

and rigid-wall conditions at the upstream and downstream boundaries are shown. Free-surface profiles at different time steps are shown (the vertical axis Y represents time). As seen in the figure, although this open boundary condition introduces some slight disturbances on the free-surface close to the boundary, it does prevent any significant reflections from affecting the results.

2.1.3. Motion of the obstacle. In the towing tank simulator, the obstacle is always towed towards the left, in the negative x-direction. The structure is started from rest with a velocity ramp where the velocity is gradually increased in a linear fashion to its final value. Careful inspection of the results for the free-surface profiles given here reveals that there are a few start-up transient waves. These transient waves are generated early in the test runs and quickly move off downstream. It was found that these transient waves do not adversely affect the results due to the long length of time for them to reach the moving obstruction and it's associated wave train.

2.1.4. Calculation of the forces. The pressure coefficient over the surface of the structure is found using the Bernoulli equation:

$$C_P = -\frac{\partial \varphi}{\partial t} - \frac{V^2}{2} - (y - \eta). \tag{11}$$

In order to evaluate the time derivative of the velocity potential φ_t on the structure, the authors observed that the time derivative of the complex velocity potential β_t is analytical in the fluid domain. Therefore, at each time step, in a manner similar to the β problem, Equation (6b) is solved for the unknown values of β_t. When solving for the time derivative β_t, on some of the boundaries φ_t is known, while on others ψ_t is known, similar to the β problem. On the free-surface φ_t is given by Equation (3) as:

$$\frac{\partial \phi}{\partial t} = -\eta - \frac{(\nabla \phi)^2}{2}.$$

On the far-field boundaries ψ_t is given by Equation (9). On the flat bottom, ψ_t is zero, while on the structure, a divided difference formula is used to evaluate ψ_t.

The lift coefficient acting on the semicircular structure is simply the integral of the pressure over the surface C_{S} of the structure:

$$C_{\mathrm{L}} = -\int_{C_{\mathrm{S}}} C_P \, \mathrm{d}x. \tag{12}$$

Applying the trapezoidal rule to the integral gives:

$$C_{\mathrm{L}} = \sum_{i=1}^{n_{\mathrm{str}}} \frac{(C_{P_i} + C_{P_{i+1}})}{2} (x_{i+1} - x_i), \tag{13}$$

where n_{str} is the number of nodes on the obstacle.

The use of the Bernoulli equation in a similar manner to find the drag has been found to produce inaccuracies due to cancellation of the pressures on opposite sides of the structure. A more accurate equation for the steady state pressure coefficient was derived under the assumption that for a given point on the obstacle, the value of the velocity potential does not change with time. Observation of the numerical results confirmed that this is a valid assumption after the first few time steps. This assumption implies:

$$\left.\frac{\partial\varphi}{\partial t}\right|_m = \frac{\partial\varphi}{\partial t} - \frac{\partial\varphi}{\partial x} U_B \approx 0$$

or

$$\frac{\partial\varphi}{\partial x} = \frac{1}{U_B}\frac{\partial\varphi}{\partial t}, \tag{14}$$

where the subscript m refers to a co-ordinate frame moving with the obstacle. In view of the no-penetration condition (4), one may write:

$$0 = -U_B \cos\vartheta + \frac{\partial\varphi}{\partial x}\cos\vartheta + \frac{\partial\varphi}{\partial y}\sin\vartheta$$

or

$$\frac{\partial\varphi}{\partial y} = \frac{U_B}{\tan\vartheta} - \frac{\partial\varphi}{\partial x}\frac{1}{\tan\vartheta}. \tag{15}$$

After substituting (14) and (15) into the Bernoulli equation, and canceling terms due to the symmetry of the obstacle, the following equation for the pressure coefficient can be found:

$$C_P = \frac{\partial\varphi}{\partial t}\left[\frac{1}{(\tan\vartheta)^2} - 1\right] - \frac{\left(\frac{\partial\varphi}{\partial t}\right)^2}{2\cdot U_B^2\cdot(\sin\vartheta)^2} - \frac{U_B^2}{2\cdot(\tan\vartheta)^2} + h, \tag{16}$$

where ϑ goes from zero at the leading edge of the structure to π at the trailing edge of the structure, U_B is the upstream Froude number, and h is the depth. Equation (16) is singular when ϑ equals zero or π. For these points, the pressure coefficient is given as:

$$C_P = \frac{U_B^2}{2} + h. \tag{17}$$

The drag coefficient at steady state may be found by taking the following integral over the surface of the obstacle:

$$C_\mathrm{d} = \int_{\vartheta=0}^{\pi} C_P\left(\vartheta, \frac{\partial\varphi}{\partial t}\right)\mathrm{d}y. \tag{18}$$

Applying the trapezoidal rule to the integral yields:

$$C_\mathrm{d} = \sum_{i=1}^{n_\mathrm{str}} \frac{(C_{P_i} + C_{P_{i+1}})}{2}(y_{i+1} - y_i). \tag{19}$$

2.1.5. Calculation of the energy in the tank. The total non-dimensional potential energy in the tank per unit tank width is found by taking the following integral over the free surface C_F:

$$\mathrm{PE} = \frac{1}{2}\int_{C_\mathrm{F}} y^2\cdot n_y\cdot\mathrm{d}s = \frac{1}{2}\int_{C_\mathrm{F}} y^2\cdot\mathrm{d}x. \tag{20}$$

This integral may be discretized to give the following finite sum:

$$\mathrm{PE} = \frac{1}{2}\sum_{i=1}^{n_l-1}(x_i - x_{i+1}) \times \left(\frac{y_i + y_{i+1}}{2}\right)^2, \tag{21}$$

where n_1 is the total number of nodes on the free-surface. The total non-dimensional kinetic energy per unit width in the tank can be found using the following formula developed by Vinje and Brevig [16]:

$$\mathrm{KE} = \frac{1}{2}\int_C \varphi \cdot \mathrm{d}\psi. \tag{22}$$

In discretized form one obtains

$$\mathrm{KE} = \frac{1}{4}\sum_{i=1}^{m_0} (\varphi_i + \varphi_{i+1}) \times (\psi_{i+1} - \psi_i), \tag{23}$$

where m_0 is the total number of nodes in the tank. The total energy in the tank is simply the sum of the kinetic and potential energies.

The drag coefficient may also be found using the principle of energy conservation in the tank at each time step. The drag coefficient may be calculated as follows:

$$C_\mathrm{d} = \frac{1}{U_B}\frac{\mathrm{d}(\mathrm{KE} + \mathrm{PE})}{\mathrm{d}t}. \tag{24}$$

This method of determining the drag coefficient agrees well with the drag coefficient obtained using Equation (19) for all cases confirming the accuracy of the numerical results. As time increases, the use of Equation (24) to evaluate the drag is not very accurate due to the loss of energy in the tank through the open boundaries.

3. NUMERICAL RESULTS

3.1. Free-surface profile

Numerical simulations were performed for values of the non-dimensional obstacle height between 0.05 and 0.9 in 0.1 increments, each for Froude numbers of 0.05, 0.15, 0.95, 2.5, and from 0.25 to 2.0 in 0.25 increments. This effort constitutes a total of 120 runs to map out the response for Froude numbers up to 2.5 and obstruction heights up to 90% of the flow depth.

Figure 4 shows the different regions of the free-surface response in the (Fn, α) parameter space. The results can be separated into two categories depending on whether or not wave breaking occurs. Due to the inviscid nature of the fluid dynamics formulation, the computations break down when a wave breaks. When this occurs, the run is shortened considerably and no steady states are approached. When wave breaking does not occur, three distinct flow regimes were identified: subcritical, transcritical and supercritical. When wave breaking occurs, it may be of any type: spilling, plunging or surging. As shown in Figure 4, surging-type breaking occurs for values of a greater than 0.7. Plunging breaking is observed in most cases, while spilling-type breaking is confined in a narrow region close to the subcritical and transcritical non-breaking regimes. Finally, in a small region in the transcritical regime, the upstream soliton breaks.

Figures 5–7 and Figures 9–12 show sample transient free-surface profile results. In these plots, the free-surface profile is shown for successive time steps. Each profile line has been displaced in the y-direction a uniform amount to give the appearance of wave motion in three dimensions, where the third dimension represents time.

3.1.1. When wave breaking does not occur. When wave breaking does not occur, three distinct flow regimes were identified: subcritical, transcritical and supercritical. The following sections describe in detail the free-surface profile characteristics for each of the flow regimes.

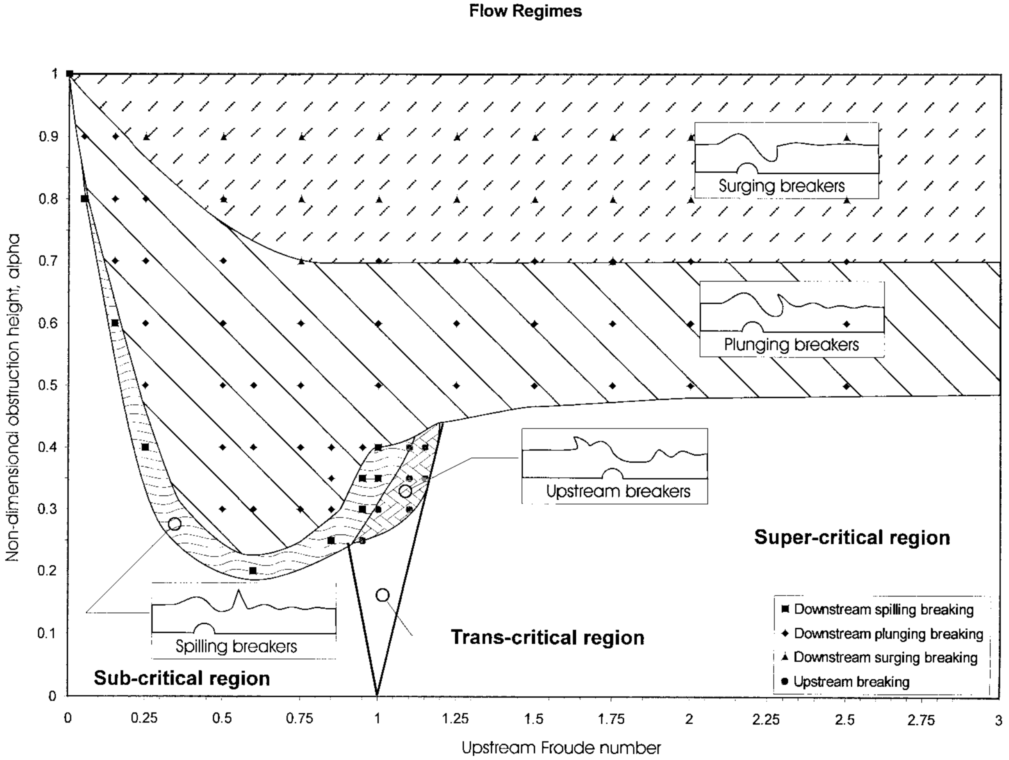

Figure 4. Free-surface flow regimes.

3.1.1.1. Subcritical. Figure 5 shows a sample free-surface profile for the subcritical case. As Figure 5 indicates, on the free-surface, solitary waves are generated upstream of the obstacle and a stationary, with respect to the obstacle, wave train develops downstream. The solitary waves are generated at a constant period while their amplitude gradually decays. As each soliton progresses upstream, its amplitude decreases while its wavelength and speed increase. Due to this increase in speed with time, the distance between successive crests in the train of solitons is always increasing. As time goes on, the amplitude of the emitted solitons decays, leaving a steady state flat free-surface profile ahead of the obstacle. As the Froude number is increased, there is a decrease in the upstream soliton emission frequency and speed.

The stationary wave train continually produces downstream waves. Growth of the wave train occurs at the far-downstream end. Initial small amplitude ripples form larger waves, matching those further upstream in the wave train. Eventually, the heights and wavelengths of these waves become steady. An oscillation is seen in the amplitude of the wave crests. As time goes on, there appears to be a long wavelength, low amplitude downstream traveling wave superimposed on the wave train.

3.1.1.2. Transcritical. In the transcritical regime, upstream solitary waves are periodically generated. The flow never reaches steady state. Figure 6 is a sample free-surface profile plot for transcritical flow. The first wave of the downstream wave train begins to move downstream. In doing so, a flat, waveless region just downstream of the obstruction is formed. The length of the flat region increases with the Froude number.

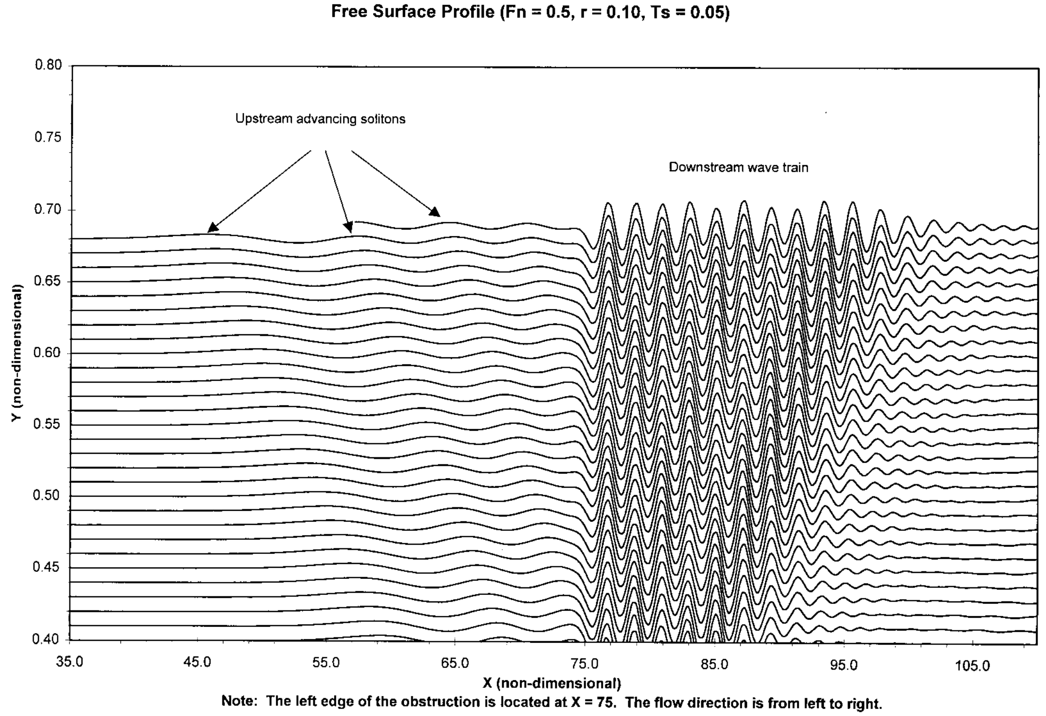

Figure 5. Sample free-surface profile plot for the subcritical case.

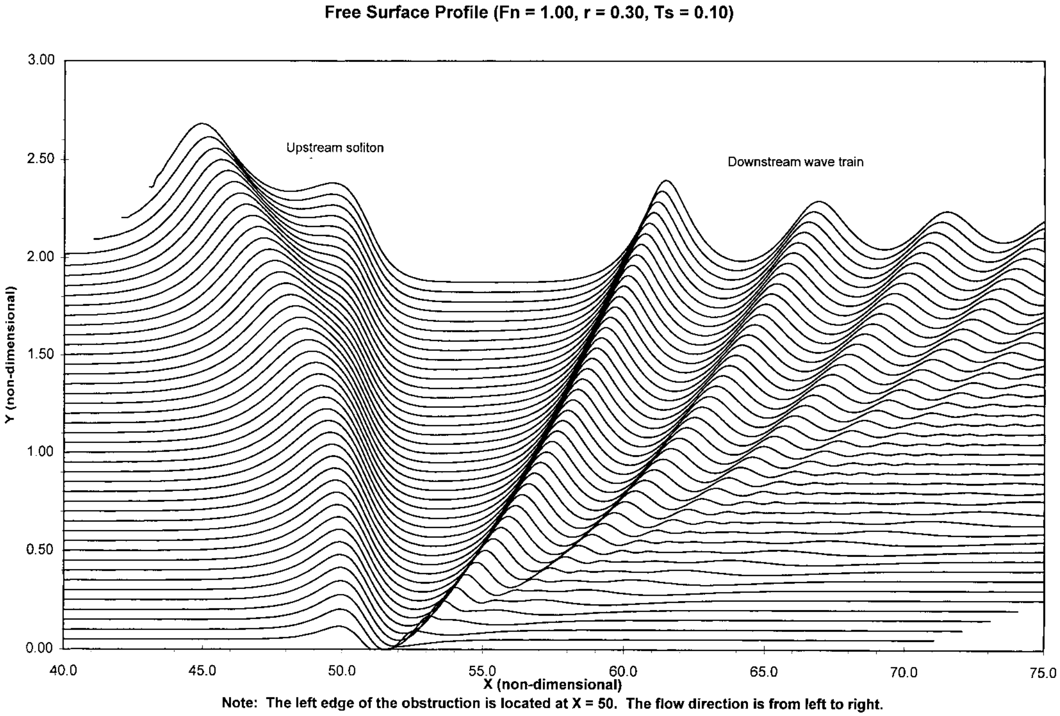

Figure 6. Sample free-surface profile plot for transcritical flow.

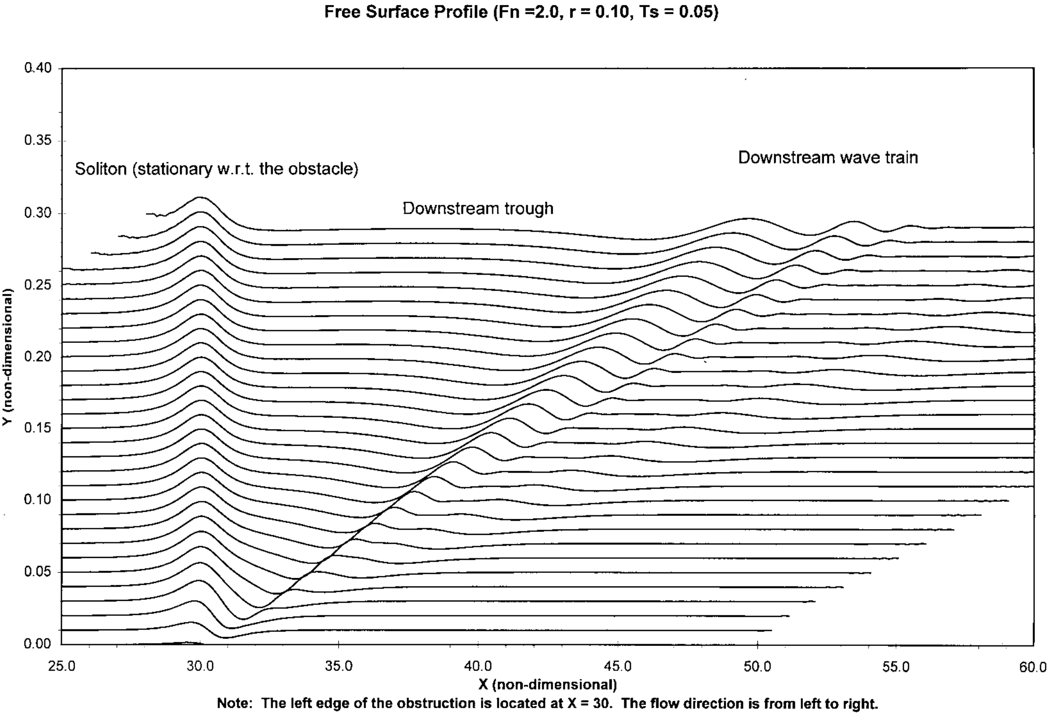

Figure 7. Sample free-surface profile plot for supercritical flow.

3.1.1.3. Supercritical. As the flow becomes supercritical, a constantly elongating trough forms behind a precursor soliton. Figure 7 is a sample free-surface profile plot for supercritical flow. Any initially produced waves are swept quickly downstream. In the steady state, the free-surface behind the obstruction is completely flat. The depth of the flat region decreases with increasing Froude number. In the case of very high Froude numbers, the free-surface returns to its initial elevation downstream of the obstacle. This is the same free-surface profile as the supercritical flow case in the steady state literature.

3.1.1.4. Overall characteristics. Figure 8 is a plot of the height of the initial upstream advancing soliton as a function of the non-dimensional obstacle height α for different values of the Froude number. In each case, the height of the soliton was measured either at steady state or when wave breaking occurred. In general, the soliton height increases with the Froude number and the obstruction height. The only exception occurs in the transcritical regime, where upstream breaking waves were encountered. In this region, the soliton height increases until it eventually forms a forward breaking wave.

3.1.2. Wave breaking

3.1.2.1. Downstream breaking. In all cases, wave breaking occurs in the first wave downstream of the obstruction. When wave breaking occurs, it may follow any pattern: spilling, plunging or surging. The transition from one breaking pattern to the other is smooth.

Spilling waves develop symmetrically. The crest becomes sharper and sharper until the peak spills to one side and the wave breaks. Plunging breakers do not form symmetrically. The crest curls over towards the obstacle and the free-surface overturns into itself. Surging breakers are seen as the collapse of a nearly vertical hydraulic jump.

Figures 9–11 show typical free-surface profiles for spilling, plunging and surging breakers respectively. When downstream plunging or surging wave breaking occurs, the wave breaks towards the obstacle. The regions where each breaking-type occurs are shown in Figure 4. The plunging-type of breaking wave dominates. As the obstruction height is increased past 0.7, the plunging wave gradually becomes a surging wave. For subcritical Froude numbers, a thin region where spilling breaking occurs exists close to the subcritical and transcritical non-breaking regimes.

3.1.2.2. Upstream breaking. Upstream breaking of the soliton occurs in a small region in the transcritical flow regime. Figure 12 shows the evolution of the free-surface for the case of upstream breaking. As shown in Figure 12, the upstream soliton grows in height and splits into two solitons. The leading soliton continues to grow in height as it moves upstream, away from the obstruction. At some distance from the obstruction it reaches a critical height and plunges forward. This type of breaking is only seen after especially long times when compared with downstream breaking. Non-dimensional times for this type of breaking begin at 30 and go up to about 55. These excessively long times are in some cases too high to be achieved in the simulation. The work performed by Zhu and Zhang [7] did not show the presence of these waves. It is suspected that the reason for this discrepancy is that sufficiently long times were not achieved in the numerical simulation to reveal upstream breaking.

3.2. *Forces on the structure*

3.2.1. Transient drag behavior. Figure 13 contains a plot of the drag on the structure, as a function of time, for subcritical flow. In subcritical flow, the drag oscillates periodically before converging to a steady state. Each of the drag maxima corresponds to the time of upstream

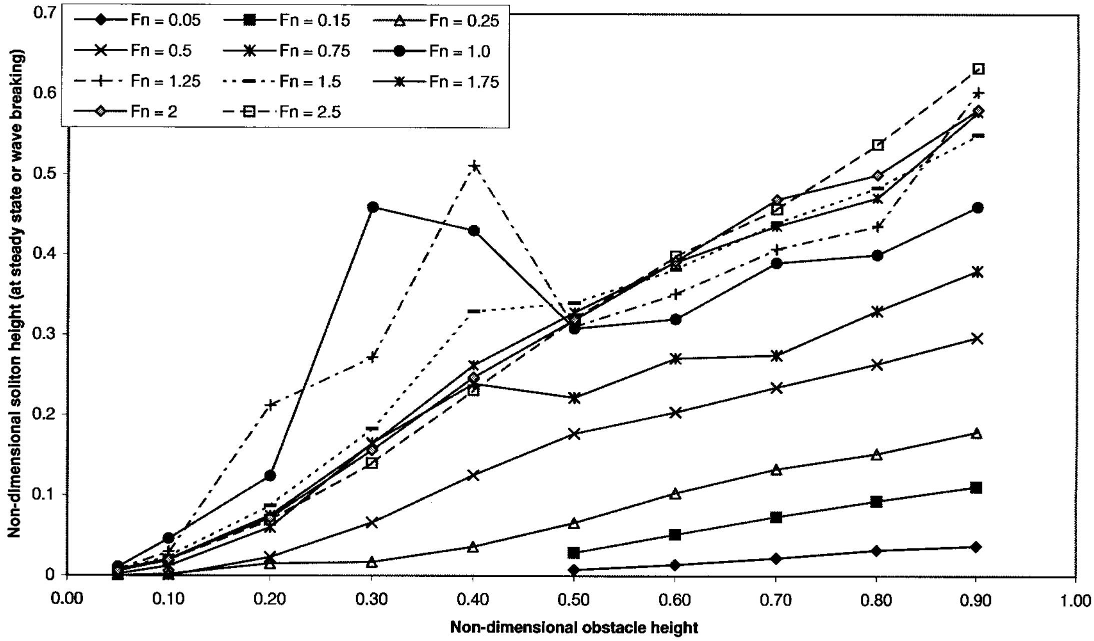

Figure 8. Plot of the height of the initial upstream advancing soliton as a function of the non-dimensional obstacle height α for different values of the Froude number.

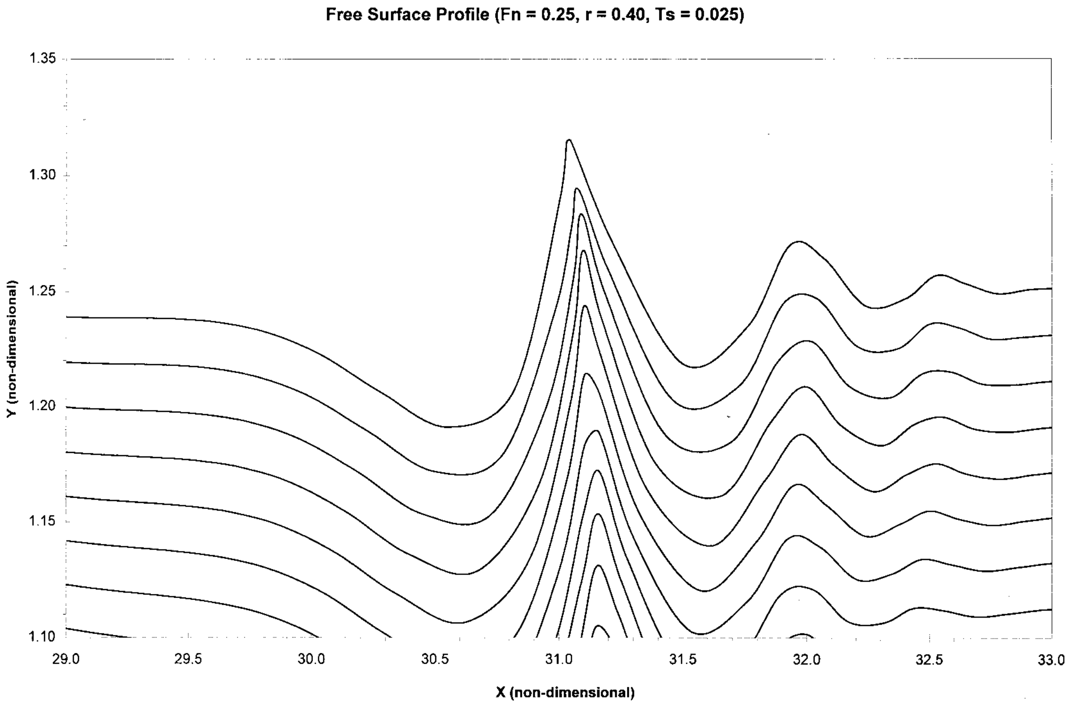

Note: The left edge of the obstruction is located at X = 30. The flow direction is from left to right.

Figure 9. Sample free-surface profile plot of a spilling-type breaking wave.

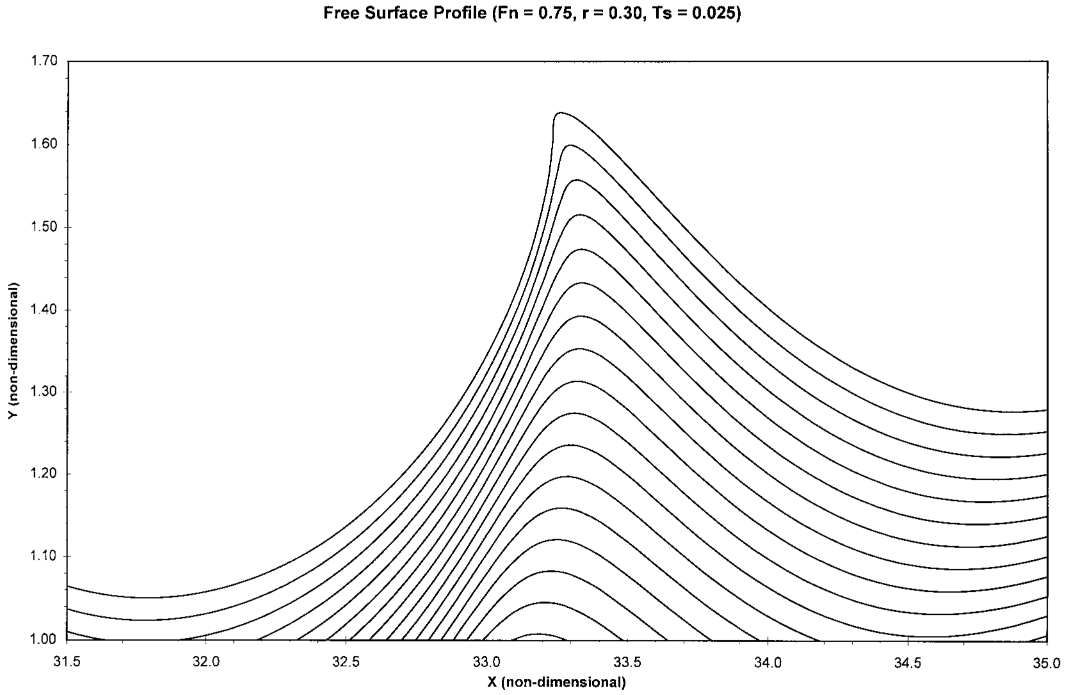

Note: The left edge of the obstruction is located at X = 30. The flow direction is from left to right.

Figure 10. Sample free-surface profile plot of a plunging-type breaking wave.

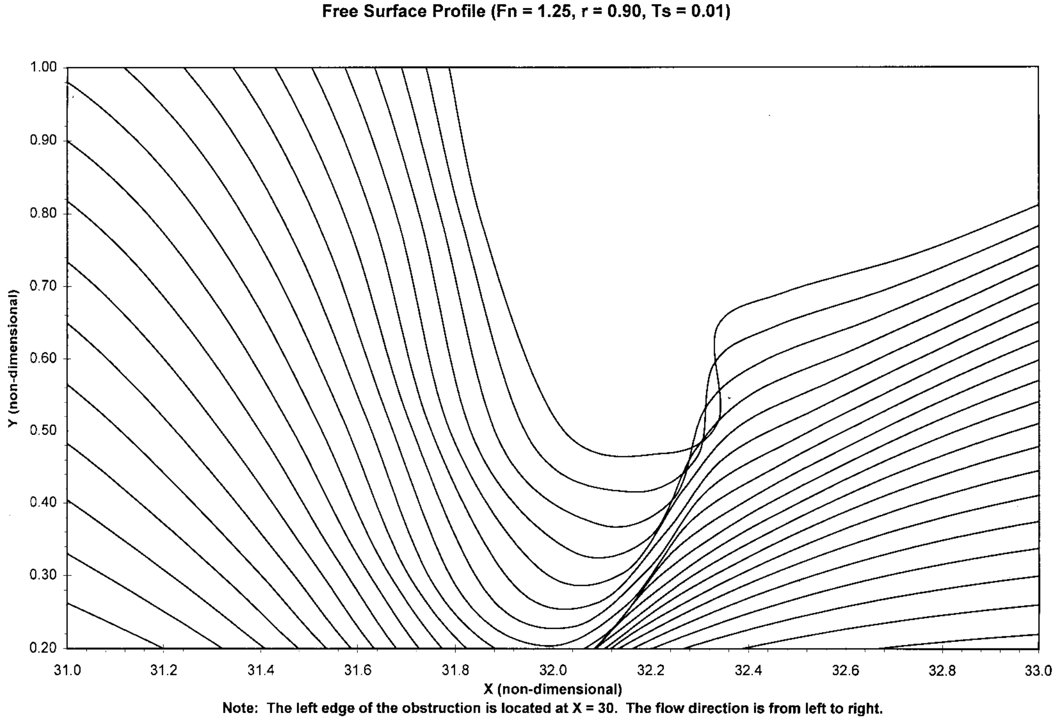

Figure 11. Sample free-surface profile plot of a surging-type breaking wave.

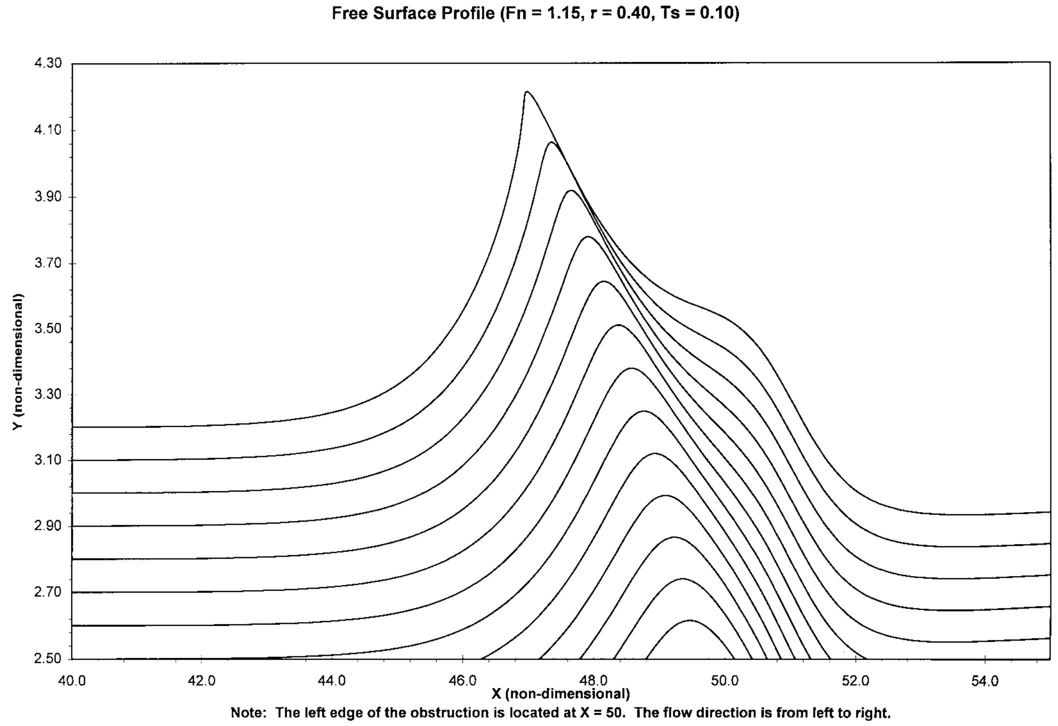

Figure 12. Sample free-surface profile plot of an upstream breaking wave.

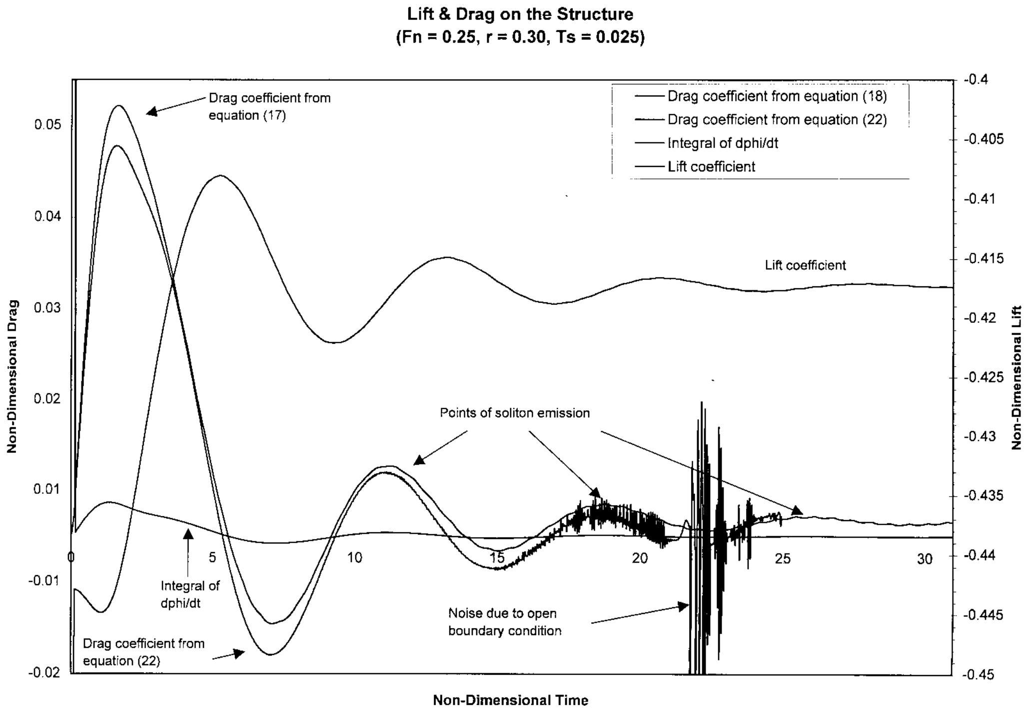

Figure 13. Plot of the lift and drag coefficients on the structure, as functions of time, for subcritical flow.

traveling soliton emission. Hence, the period of the oscillations in the drag is equal to the soliton emission period. As mentioned earlier, this period increases as the Froude number increases. The amplitude of these oscillations goes to zero as the height of the solitons decay to zero. After a sufficiently long time, the drag converges to a steady state.

Also shown in Figure 13 is a plot of the $\partial\varphi/\partial t$ term. It is seen that this term is negligible after the first few time steps. This verifies the validity of the assumption leading to Equation (14).

Figure 14 contains a plot of the drag on the structure, as a function of time, for supercritical flow. In supercritical flow, the drag goes through an initial maximum, before slowly decaying to a steady state. No periodic oscillations are seen in the drag in the supercritical regime. When wave breaking occurs, the transient behavior described above is simply truncated at the point where the wave breaks.

3.2.2. Steady state drag. In the subcritical and supercritical regimes, when no wave breaking occurs, the solution for the drag will converge to a steady state after a sufficiently long time. In general, for very high supercritical and low subcritical Froude numbers, the drag converges quickly. As the Froude number approaches the transcritical regime (from either side) the rate of convergence decreases rapidly.

Figure 15 is a plot of the steady state drag as a function of non-dimensional obstacle height for various Froude numbers. Higher obstacle heights always produce more drag than lower ones at the same Froude number. It appears that the steady state drag is exponentially related to the height of the obstacle. In the case of subcritical flow, the steady state drag increases with the Froude number. For example, the steady state drag for an obstruction height that is 20%

of the flow depth is about 23 times greater for a Froude number of 0.5 than for a Froude number of 0.25.

In the supercritical flow regime, the steady state drag actually decreases as the Froude number is increased. It is also possible for the drag for supercritical flow to be less than that for subcritical flow, for equal obstruction heights. The steady state drag for a Froude number of 1.50 is about 3.9 times greater than that for a Froude number of 2.5, at a non-dimensional obstacle height of 0.40.

3.2.3. Transient lift behavior. Periodic oscillations are seen in the lift for subcritical flow. These oscillations are about 90° out of phase with the oscillations in the drag. After a sufficiently long time, the amplitude decays to a steady state value. Figure 13 contains a sample plot of the lift as a function of time for subcritical flow. Note that the lift in some cases is negative. This is due to the strong negative contribution of the hydrostatic pressure to the lift. In subcritical flow, the hydrostatic contribution to the lift can be as much as 96% of the total.

In the supercritical flow case, the lift goes through a sharp initial maximum before decaying to a steady state. Figure 14 is a sample plot of the lift as a function of time for supercritical flow. In supercritical flow, the hydrostatic contribution can be as much as 55% of the total lift.

3.2.4. Steady state lift. Figure 16 is a plot of the steady state lift as a function of the structure for various Froude numbers. In the case of supercritical flow, the steady state lift appears to go through a maximum value at some obstruction height. The location of this maximum appears to shift toward higher values of the obstacle height with increasing Froude number. For subcritical flow, on the other hand, the lift always decreases with increasing obstacle height. In all cases, the lift is higher for higher Froude numbers.

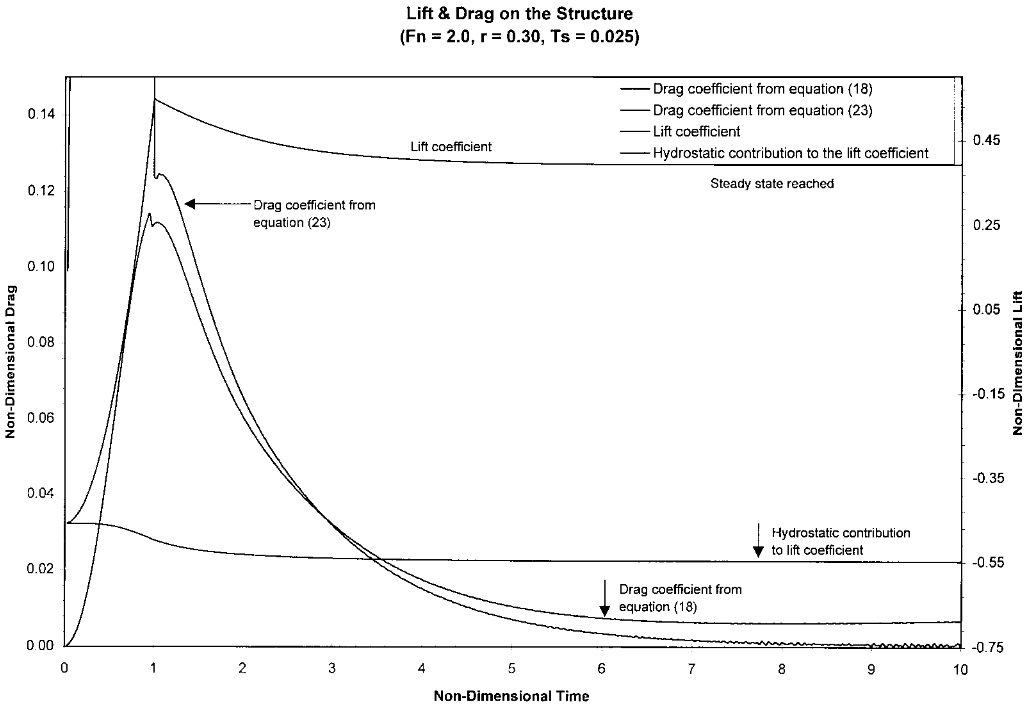

Figure 14. Plot of the lift and drag coefficients on the structure, as functions of time, for supercritical flow.

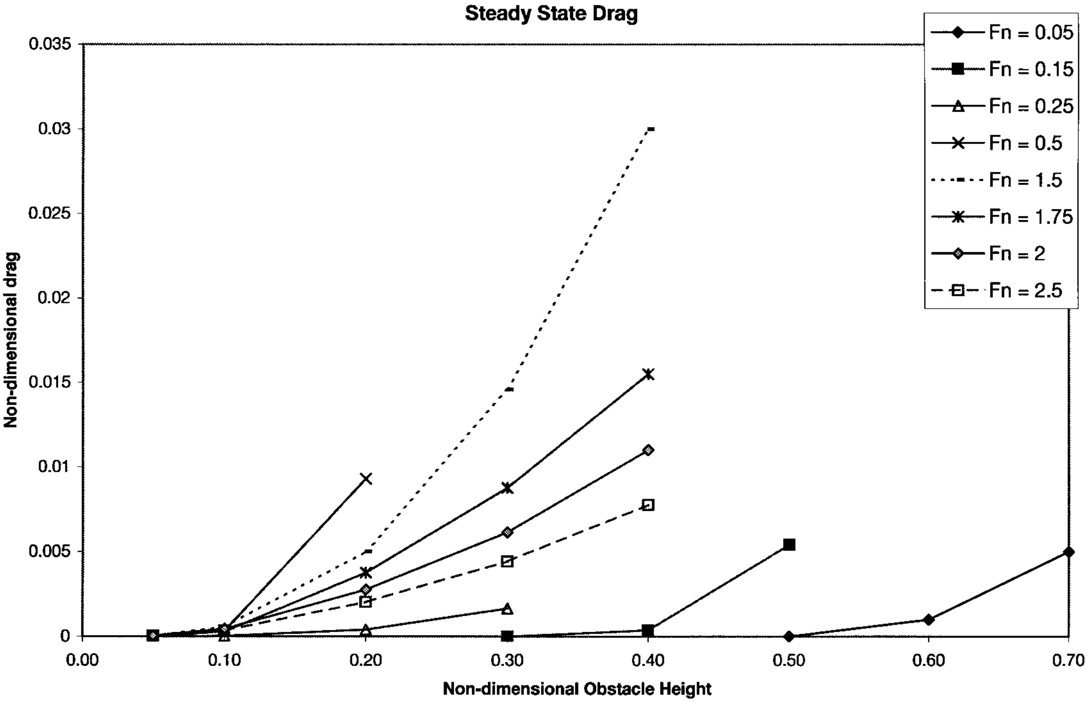

Figure 15. Plot of the steady state drag as a function of non-dimensional obstacle height for various Froude numbers.

4. CONCLUSIONS

Extensive numerical simulations were carried out to study the non-linear free-surface flow over a bottom obstruction in two dimensions. A mixed Eulerian–Lagrangian numerical method was employed. The problem was solved in the time domain that allows the prediction of a number of transient phenomena that cannot be predicted by steady flow models. Such phenomena include the generation of upstream advancing solitary waves as well as the simulation of wave breaking. A parametric study was performed for a range of values of the depth-based Froude number up to 2.5 and non-dimensional obstacle heights, α, up to 0.9. Different breaking and non-breaking flow regimes were identified. When wave breaking does not occur, three distinct flow regimes were identified: subcritical, transcritical and supercritical. In the subcritical case, a train of solitary waves is generated upstream of the obstacle and a stationary, with respect to the obstacle, wave train develops downstream. In the transcritical regime, upstream solitary waves are periodically generated. The flow never reaches steady state. The first wave of the downstream wave train begins to move downstream. In doing so a flat, waveless region just downstream of the obstruction is formed. The length of the flat region increases with the Froude number. As the flow becomes supercritical, a constantly elongating trough forms behind a precursor soliton. Any initially produced waves are swept quickly downstream. In the steady state, the free-surface behind the obstruction is completely flat. The depth of the flat region decreases with increasing Froude number. In the case of very high Froude numbers, the free-surface returns to its initial elevation downstream of the obstacle.

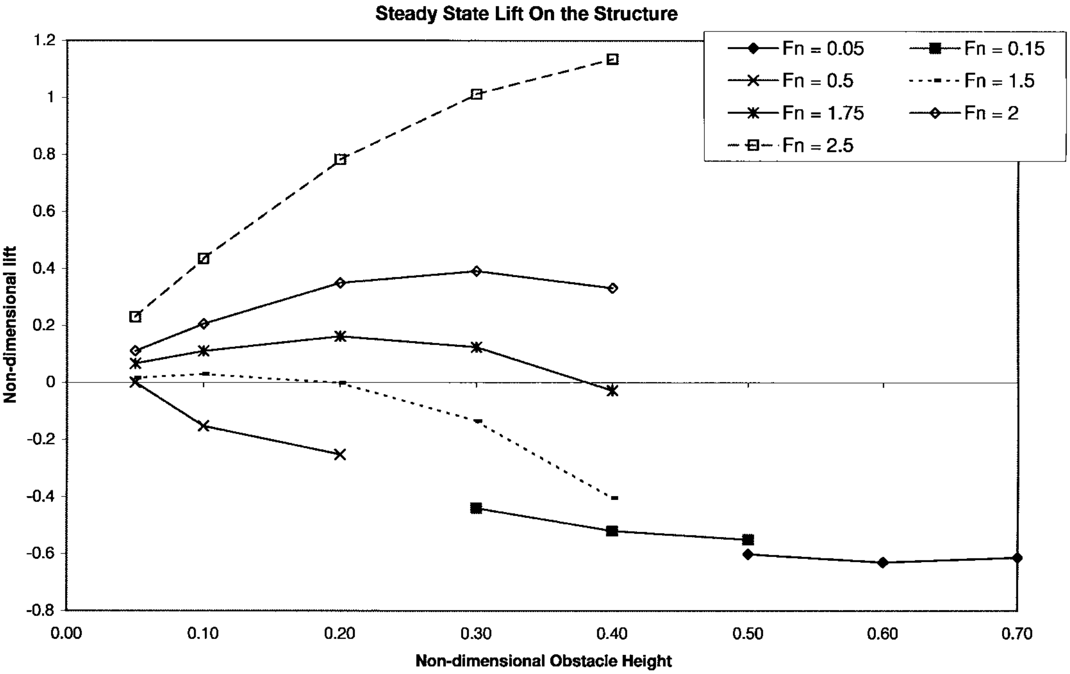

Figure 16. Plot of the steady state lift as a function of the structure for various Froude numbers.

When breaking occurs it may be of any type: spilling, plunging or surging. In addition, for values of the Froude number close to 1, the upstream solitary waves break. A systematic study was undertaken to define the boundaries of each type of flow pattern and to determine the drag and lift coefficients, free-surface profile characteristics and transient behavior.

ACKNOWLEDGMENTS

The authors would like to acknowledge Premkumar Muthedath and Linda Constantine for their assistance in developing the numerical code. They would also like to thank Jeff Cullina and Jason Dare for their help in performing the multitude of test runs required for the parametric study. This research was partially supported by a grant from the National Science Foundation (Grant No. CMS-942248).

REFERENCES

1. L.K. Forbes, 'Critical free-surface flow over a semi-circular obstruction', *J. Eng. Math.*, **22**, 3–13 (1988).
2. L.K. Forbes and L.W. Schwartz, 'Free-surface flow over a semicircular obstruction', *J. Fluid Mech.*, **114**, 299–314 (1982).
3. Y. Zhang and S. Zhu, 'Open channel flow past a bottom obstruction', *J. Eng. Math.*, **30**, 487–499 (1996).
4. J.M. Vanden-Broeck, 'Free-surface flow over an obstruction in a channel', *Phys. Fluids*, **30**, 2315–2317 (1987).
5. D.D. Houghton and A. Kasahara, 'Non-linear shallow fluid flow over an isolated ridge', *Commun. Pure Appl. Math.*, **21**, 1–23 (1968).
6. G.A. Lawrence, 'Steady flow over an obstacle', *J. Hydraul. Eng.*, **113**, 981–991 (1987).
7. S. Zhu and Y. Zhang, 'On non-linear transient free-surface flows over a bottom obstruction', *Phys. Fluids*, 1996 (submitted).
8. J.G. Thews and L. Landweber, 'The influence of shallow water on the resistance of a cruiser model', US Experimental model basin, Navy Yard, Washington DC, Report No. 408, p. 31, 1935.

9. D.-M. Wu and T.Y. Wu, 'Three-dimensional non-linear long waves due to moving surface pressure', *Proc. 14th Symp. Naval Hydrodynamics*, Ann Arbor, MI, pp. 103–129, 1982.
10. T.R. Akylas, 'On the excitation of long non-linear water waves by a moving pressure distribution', *J. Fluid Mech.*, **141**, 455–466 (1984).
11. S.L. Cole, 'Transient waves produced by flow past a bump', *Wave Motion*, **7**, 579–587 (1985).
12. C.C. Mei, 'Radiation of solitons by slender bodies advancing in a shallow channel', *J. Fluid Mech.*, **162**, 53–67 (1986).
13. R.C. Ertekin, W.C. Webster and J.V. Wehausen, 'Waves caused by a moving disturbance in a shallow channel of finite width', *J. Fluid Mech.*, **169**, 275–292 (1986).
14. Y. Cao, R.F. Beck and W.W. Schultz, 'Numerical computations of two-dimensional solitary waves generated by moving disturbances', *Int. J. Numer. Methods Fluids*, **17**, 905–920 (1993).
15. M.S. Longuet-Higgins and E.D. Cokelet, 'The deformation of steep surface waves on water', *Proc. R. Soc. Lond. A*, **350**, 1–26 (1976).
16. T. Vinje and P. Brevig, 'Breaking waves on finite water depths. A numerical study', The Ship Research Institute of Norway, 1981.
17. W.M. Lin, 'Non-linear motion of the free-surface near a moving body', *Ph.D. Thesis*, Massachusetts Institute of Technology, Cambridge, MA, 1984.
18. R. Cointe, 'Non-linear simulation of transient free-surface flows', *Proc. 5th Int. Conf. on Numerical Ship Hydrodynamics*, Hiroshima, Japan, pp. 239–250, 1989.
19. P. Muthedath, 'Numerical study of non-linear free-surface flows', *MS Thesis*, Virginia Polytechnic Institute and State University, Blacksburg, VA, 1992.
20. S. Grilli and J. Horrillo, 'Numerical generation and absorption of fully non-linear periodic waves', *J. Eng. Mech.*, **123**, 1060–1069 (1997).
21. A. Van Dongeren and I. Svendsen, 'Absorbing–generating boundary condition for shallow water models', *J. Waterway Port coast. Ocean Eng.*, **123**, 303–313 (1997).
22. I. Orlanski, 'A simple boundary condition for unbounded hyperbolic flows', *J. Comput. Phys.*, **21**, 251–269 (1976).
23. T.Y. Han, J.C.S. Meng and G.E. Innis, 'An open boundary condition for incompressible stratified flows', *J. Comput. Phys.*, **49**, 276–297 (1983).